ACS APPLIED MATERIALS & INTERFACES

Research Article

Cite This: ACS Appl. Mater. Interfaces 2018, 10, 5949−5958

www.acsami.org

Layer-by-Layer Epitaxial Growth of Defect-Engineered Strontium Cobaltites

Tassie K. Andersen,[*,§,†] Seyoung Cook,[§,†] Gang Wan,[§] Hawoong Hong,[‡] Laurence D. Marks,[†] and Dillon D. Fong[§]

[§]Materials Science Division, Argonne National Laboratory, Argonne, Illinois 60439, United States

[†]Department of Materials Science and Engineering, Northwestern University, Evanston, Illinois 60208, United States

[‡]Advanced Photon Source, Argonne National Laboratory, Argonne, Illinois 60439, United States

ABSTRACT: Control over structure and composition of (ABO_3) perovskite oxides offers exciting opportunities since these materials possess unique, tunable properties. Perovskite oxides with cobalt B-site cations are particularly promising, as the range of the cation's stable oxidation states leads to many possible structural frameworks. Here, we report growth of strontium cobalt oxide thin films by molecular beam epitaxy, and conditions necessary to stabilize different defect concentration phases. In situ X-ray scattering is used to monitor structural evolution during growth, while in situ X-ray absorption near-edge spectroscopy is used to probe oxidation state and measure changes to oxygen vacancy concentration as a function of film thickness. Experimental results are compared to kinetically limited thermodynamic predictions, in particular, solute trapping, with semiquantitative agreement. Agreement between observations of dependence of cobaltite phase on oxidation activity and deposition rate, and predictions indicates that a combined experimental/theoretical approach is key to understanding phase behavior in the strontium cobalt oxide system.

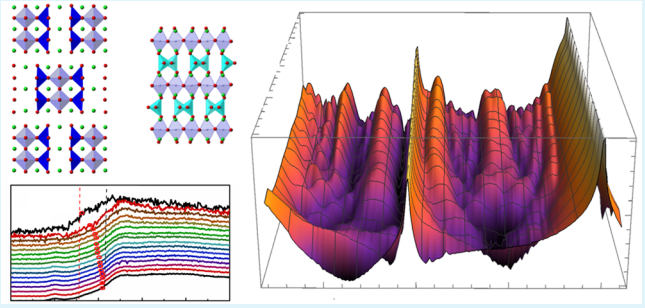

KEYWORDS: *metal oxides, strontium cobalt oxide, molecular beam epitaxy, defects in oxides, perovskite oxides, thin films*

INTRODUCTION

The demand for improved performance in energy conversion and storage devices, including solid oxide fuel cells and electrocatalysts,[1−4] as well as "beyond Moore" information processing technologies,[5,6] necessitates the design and synthesis of new materials. Perovskite-derived transition metal oxides are particularly well suited to addressing these challenges because they offer an enormously wide range of electronic, magnetic, and optical properties, all within a common ABO_3 structural framework.[7] The intimate relationship between the *d* orbitals of the B-site ion and the 2*p* oxygen orbitals within the BO_6 octahedron allows fine-scale tuning of these behaviors and even coupling among different properties through application of an external field.[8] A more recent realization was the importance of functional ion defects in these materials,[9] highlighting the critical need for control over point defects within the different ionic sublattices. In addition, for perovskites with multivalent B-site cations, oxygen vacancies play an especially important role in determining the electrochemical properties of the oxide.[10−12]

A particularly versatile B-site transition metal is cobalt because it exhibits oxidation states varying from 2+ to 4+ and therefore a range of different coordination environments with oxygen (tetrahedral, square pyramidal, and octahedral). This allows the creation of many possible structural frameworks, each with unique physicochemical properties, all dependent on the oxygen vacancy concentration. A wide range of interesting properties have been exhibited in the cobalt oxides, including high electrocatalytic activity,[12,13] reversible magnetic states,[14] and controllable oxygen diffusivity,[15] all of which has led to significant interest in the controlled synthesis of these materials.[12,16,17] For instance, $SrCoO_3$ is a ferromagnetic metal comprised entirely of corner-shared octahedra,[18] while $SrCoO_{2.5}$ is an antiferromagnetic insulator made from both tetrahedral and octahedral building blocks. The similarity between the $SrCoO_3$ and $SrCoO_{2.5}$ crystal structures permits fully reversible oxygen intercalation between the two phases via a topotactic phase transition,[3,12,19−22] enabling redox-based tuning of material properties.

Controlling oxygen nonstoichiometry in the strontium cobaltites through experimental methods and conditions during epitaxial thin film synthesis offers another route to achieving defect-engineered properties in these materials. Oxygen vacancies order to form the homologous series $SrCoO_{(3n-1)/n}$, with n = 2, 4, 8, and ∞, the $SrCoO_3$ endmember, structures having been reported.[20,23,24] These structures are shown in Figure 1a−d, where brownmillerite-structured (BM-SCO)

Received: November 7, 2017
Accepted: January 18, 2018
Published: January 18, 2018

DOI: 10.1021/acsami.7b16970
ACS Appl. Mater. Interfaces 2018, 10, 5949−5958

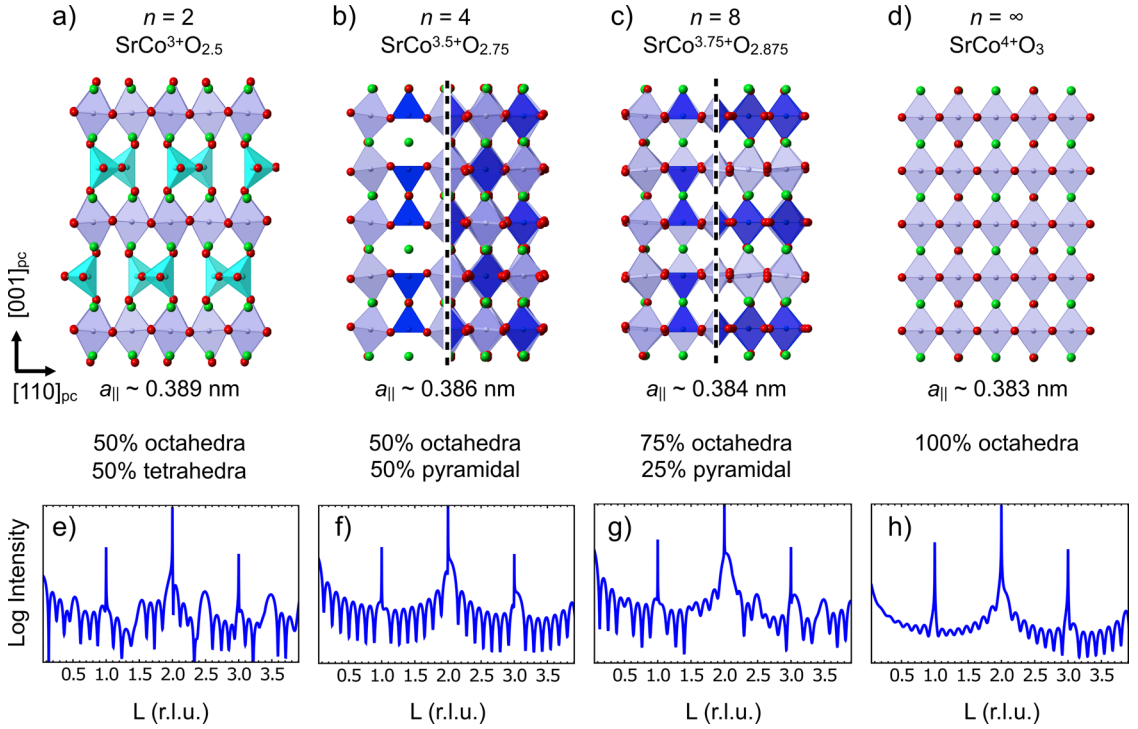

Figure 1. Structures of the stable members of the $SrCoO_{(3n-1)/n}$ homologous series for n = 2 (a), 4 (b), 8 (c), and ∞ (d) on $SrTiO_3$ (001) and (e−h) their corresponding (calculated) X-ray scattered intensities along the (00L) specular rod assuming films are coherently strained, respectively. The n = 4 and 8 members (b and c) have two possible orientations, shown separated by the dotted line, the (00L) in panels f and g are an average of these two. The polyhedra corresponding to CoO_4, CoO_5, and CoO_6 are shown in cyan, blue, and violet, respectively. Strontium atoms and oxygen atoms are green and red, respectively. The defect structures are expected to evolve from left to right when moving from reducing to more oxidizing conditions.

$SrCoO_{2.5}$ and perovskite-structured (P-SCO) $SrCoO_3$ correspond to n = 2 and ∞, respectively. Within this defect structure series, controlling growth parameters leads to a range of attainable Co oxidation states increasing from Co^{3+} to Co^{4+} accompanied by a decrease in the in-plane (pseudocubic) lattice parameter, $a_{||}$, with increasingly oxidizing conditions.[20] Both oxygen activity and epitaxial strain play key roles in phase determination, and it was previously demonstrated that one can even select a particular n and intermediate oxygen stoichiometries by applying epitaxial strain using different single-crystal substrates.[3] The degree of oxygen vacancy ordering can be easily measured through X-ray diffraction, with the corresponding (00L) specular rod intensities for the structures in Figure 1a−d shown in Figure 1e−h, respectively. Previous strontium cobalt oxide films were grown by pulsed laser deposition (PLD), which takes place in a dense plasma environment with particle impingement energies ranging from 5 eV to over 50 eV; the films were therefore grown in conditions very far from thermal equilibrium.[3,10,12,19,22,25,26] In contrast, the impingement energies for molecular beam epitaxy (MBE) are on the order of 0.1 eV,[27] and the growth rates are much slower than those of PLD, allowing for much greater control over the construction of each individual atomic layer, including its defect content.[28] Since one of the goals of this study was to understand the structure of films at the individual atomic monolayer level the flexibility and control afforded by MBE led to its choice as the method of synthesis.

However, the growth conditions for stabilizing different members of the $SrCoO_{(3n-1)/n}$ series and their related defect-ordered structures are not well-known for MBE synthesis. These conditions must be identified to reliably grow materials that take advantage of the tunable properties available in the strontium cobalt oxide system to facilitate their integration into functional devices. Here, we report a systematic investigation into the growth of strontium cobalt oxide (SCO) thin films by oxide MBE. We exploit a unique instrument that permits both in situ X-ray scattering and absorption spectroscopy during growth, allowing detailed observations of the atomic-scale processes that take place during reactive deposition and the evolution of oxygen defects and defect ordering within the growing film.[29] We determine the optimal MBE conditions for stabilization of different SCO phases and compare our results with calculated thermodynamic equilibria and kinetically limited thermodynamic processes such as solute trapping.[30−33]

Applying these approaches allows the effects of growth conditions to be understood from a theoretical viewpoint. This in turn enables prediction of the conditions necessary for growth of defect-engineered films via MBE.

EXPERIMENTAL SECTION

Thin Film Deposition. The SCO films were grown on low miscut (<0.1°) single-crystal 10 mm × 10 mm × 1 mm $SrTiO_3$ (0 0 1) substrates (CrysTec GmbH) chemically prepared to exhibit TiO_2 surface termination.[34] The crystals were first sonicated in deionized water for 10 min at room temperature and agitated in a buffered hydrofluoride solution (NH_4F:HF = 3:1) of pH 5−5.5 for 30 s before being rinsed in deionized water. The etched substrates were then annealed at 1323 K for 2 h in flowing oxygen, resulting in terraced surfaces that exhibited unit-cell height steps. All films were grown by reactive molecular beam epitaxy using the custom-built chamber shown schematically in Figure 2. Pure oxygen or oxygen mixtures with ozone collected from a commercial distiller (DCA Instruments) was introduced into the chamber using a leak valve and controlled at total

DOI: 10.1021/acsami.7b16970
ACS Appl. Mater. Interfaces 2018, 10, 5949−5958

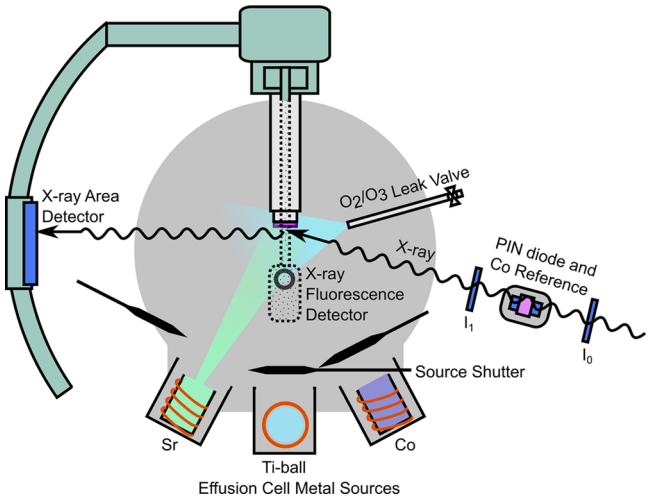

Figure 2. Schematic of the oxide MBE and surface X-ray scattering chamber at sector 33-IDE of the APS showing the geometry of growth, in situ scattering and in situ spectroscopy measurements.

pressures ranging from 2.67×10^{-5} to 1.33×10^{-4} Pa. The relative ozone concentration was varied from 10% (i.e., 10% O_3 + 90% O_2) to nominally 100%. Prior to deposition, the substrates were annealed for 20 min in the background O_2/O_3 environment at a substrate temperature, T_{sub}, that ranged from 823 to 1023 K as measured by an optical pyrometer. The strontium and cobalt metal vapors were supplied via effusion cells with fluxes calibrated by a quartz crystal microbalance. We used a sequential deposition method in the pattern Sr → Co → Sr → Co → etc., where the shutters of the individual effusion cells were programmed to open and close after the deposition of each single atomic plane or monolayer (ML). This shutter order was chosen to produce either the Brownmillerite or the perovskite phases.[35−37]

In Situ X-ray Scattering. The MBE chamber is mounted on a six-circle diffractometer, as shown in Figure 2, and installed at Sector 33-IDE of the Advanced Photon Source (APS).[38] A curved beryllium window allows X-rays to enter and exit the MBE chamber for scattering measurements. During shuttered deposition, we monitored the evolution of scattered X-ray intensity at the anti-Bragg position (001/2) of the $SrTiO_3$ substrate, which provides information on the film thickness and growth mode,[39] and measured the (00L) specular rod immediately following deposition. Some films were interrupted periodically during growth to perform (00L) specular measurements, which provides detailed information on film evolution. (Here, we employ reciprocal lattice units (rlu) referenced to the room temperature $SrTiO_3$ lattice parameter, 0.3905 nm, and use pseudocubic (pc) indexing for all crystal structures.) Two-dimensional images of the scattered 7.5 keV X-rays were recorded with a pixel array detector (Pilatus 100 K, Dectris) and reduced to background-subtracted integrated intensities.[40]

In Situ X-ray Absorption Spectroscopy. To determine the oxidation state of Co during the growth of SCO on $SrTiO_3$, we also performed in situ X-ray absorption near-edge structure (XANES) measurements across the Co K-edge. The intensity of the fluoresced X-rays from the SCO films was measured with a silicon drift detector (Vortex-60EX, Hitachi) aimed at the sample from above, as shown in Figure 2, such that the X-rays passed through the beryllium exit window. To calibrate the X-ray energy, parasitic air scattering from the incident beam was transmitted through a 5-μm-thick Co reference foil placed atop a Si-PIN photodiode. In front of the reference foil was an ionization chamber, providing incident intensity I_0, which was used to normalize reference spectra. Downstream from the reference a second ion chamber, measuring intensity I_1, was placed, allowing normalization of sample spectra.

RESULTS AND DISCUSSION

Sr−Co−O Film Growth. Epitaxial growth of cobalt oxides by MBE requires maintaining a narrow substrate temperature and background pressure window—the temperature must be high enough to achieve sufficient adatom mobilities (>∼773 K) but low enough to prevent decomposition of the film into the hexagonal $Sr_6Co_5O_{15}$ phase (∼923 K for bulk systems).[41] Although the total background pressure is limited to a maximum of $\sim 10^{-4}$ Pa, changing the O_2 to O_3 ratio varies the oxygen activity by many orders of magnitude (up to 10^{15} depending on the temperature). Within the investigated temperature and oxygen activity window, we observed the appearance of two distinct crystalline phases, both of which were epitaxial with the $SrTiO_3$ (001) substrate; measurements of nonspecular Bragg peaks indicated that both phases were also coherently strained to the substrate. The scattered intensities along the specular rod for these phases are shown in Figure 3a, b, and the XANES spectra are presented in Figure 3c. The latter shows that for both phases, Co has an oxidation state of 3+. The crystal structure in Figure 3a can be readily identified by reference to Figure 1e as brownmillerite, $SrCoO_{2.5}$. The film shown was grown at T_{sub} = 875 K with 100% O_3 delivered at $pO_3 = 1.33 \times 10^{-4}$ Pa. The results are in good agreement with previous reports for PLD-grown $SrCoO_{2.5}$

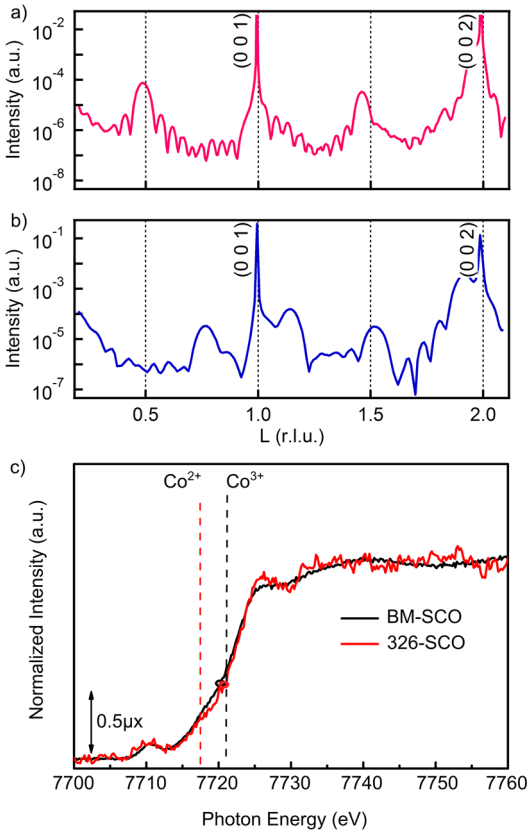

Figure 3. X-ray scattering along the (00L) crystal truncation rod of phase-pure $SrCoO_{2.5}$ (a) and $Sr_3Co_2O_{6\pm\delta}$ (326-SCO) (b) films grown on $SrTiO_3$ (001). Film shown in panel a was grown at T_{sub} = 875 K, $pO_3 = 1.33 \times 10^{-4}$ Pa, and that shown in panel b was grown at T_{sub} = 873 K, $pO_2 = 1.33 \times 10^{-4}$ Pa. XANES at the Co K-edge (c) for the films, showing they both exhibit $\sim Co^{3+}$, as measured at μx = 0.5 (the intensity halfway point of normalized spectra). The energy references are from the Co metal foil and refs 43 and 44.

DOI: 10.1021/acsami.7b16970
ACS Appl. Mater. Interfaces 2018, 10, 5949−5958

films that possess a pseudotetragonal structure with in-plane and out-of-plane lattice parameters of a_t = 0.3905 nm and $c_{t/4}$ = 0.3940 nm, respectively (at room temperature).[42] The scattering data in Figure 3a show reflections near the substrate Bragg peaks as well as superstructure reflections at (00m/2), with m being odd, stemming from octahedral-tetrahedral stacking along $[001]_{pc}$, as shown in Figure 1a.

The scattering pattern in Figure 3b does not match any of those shown in Figure 1e–h, suggesting that the structure is not a member of the BM-SCO to P-SCO series, $SrCoO_{(3n-1)/n}$. This film was grown at T_{sub} = 873 K, but using 100% O_2 delivered at $pO_2 = 1.33 \times 10^{-4}$ Pa. There are numerous Sr–Co–O phases,[45] but only a small number would be coherently strained with the $SrTiO_3$ (001) substrate, like those observed herein. These include the perovskite-related Ruddlesden–Popper series, $Sr_{n+1}Co_nO_{3n+1}$.[46] We note that Ruddlesden–Popper films of similar A–B–O oxide materials have previously been grown on perovskite-type substrates. These films have been shown to be stable and coherently strained to the substrate, in many cases forming intergrowths with each other or the perovskite endmember of their respective series.[47−49] Considering that only the first few n members would be structurally stable, we consider Sr_2CoO_4, $Sr_3Co_2O_7$, and $Sr_4Co_3O_{10}$, which have bulk out-of-plane lattice constants of 1.233, 2.022, and 2.855 nm, respectively. The period of the film Bragg peaks in Figure 3b is ∼0.385 in L or 1.01 nm in real space. This agrees only with $Sr_3Co_2O_7$, given that the Bragg condition is satisfied for every (002) plane in the tetragonal unit cell (Figure 4a). However, the Co^{3+} observed in XANES

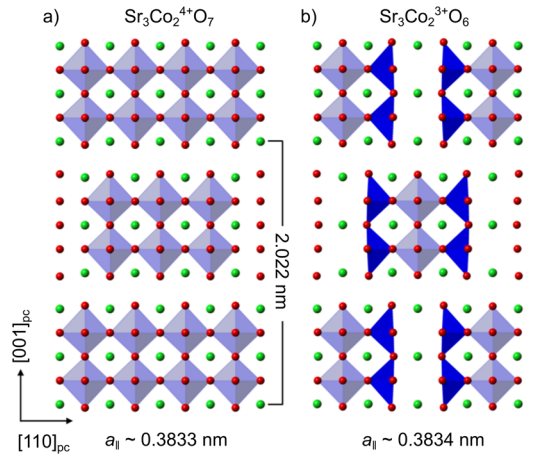

Figure 4. Crystal structures of the $Sr_3Co_2O_7$ Ruddlesden–Popper (a) and the related oxygen-deficient $Sr_3Co_2O_{6\pm\delta}$ (b) showing positions of oxygen vacancies. The polyhedra corresponding to CoO_5 and CoO_6 are shown in blue and violet, respectively. Strontium atoms and oxygen atoms are shown in green and red, respectively.

indicates that the actual stoichiometry is closer to $Sr_3Co_2O_{6\pm\delta}$ (326-SCO), where $6 \pm \delta$ indicates a number close to 6, within the error of the measurement. Synthesis of bulk samples of $Sr_3Co_2O_{5.78}$, $Sr_3Co_2O_{5.91}$, $Sr_3Co_2O_{5.94}$, and $Sr_3Co_2O_{6.06}$ have all been reported in literature, and their structures have been determined.[50,51] As shown in Figure 4b, oxygen vacancy ordering also occurs in this system, forming lattice frameworks comprised of CoO_5 square pyramids and CoO_6 octahedra.[50]

All films grown across the explored range of conditions were identified as either $SrCoO_{2.5}$ $(001)_{pc}$, $Sr_3Co_2O_{6\pm\delta}$ $(001)_{pc}$, or a mixture of the two. Some films, particularly those identified as pure $Sr_3Co_2O_{6\pm\delta}$, also exhibited diffraction peaks at (0, 0, L = 1.83), indicating the presence of (001)-oriented CoO particles. Since the deposition ratio of Sr:Co was approximately one for all samples, some amount of CoO is expected. In most instances, however, there was no trace of CoO. This could potentially be due to volatilization of CoO nanoparticles, an explanation offered for other oxide materials.[52] However, the vapor pressure of CoO at the growth temperatures investigated is very low, making this unlikely. The phenomenon of solute trapping offers a possible explanation and will be discussed in later sections. We note that one or both of the $SrCoO_{2.5}$ and $Sr_3Co_2O_{6\pm\delta}$ compounds may be stable over some A:B composition range. As the bulk Sr–Co–O phase diagram has only recently been investigated,[45,53] the upper limits of nonstoichiometry in the two compounds are currently unclear, particularly for thin film samples.

Effects of Growth Rate on Phase Stability. To investigate the role of growth kinetics on phase behavior, we conducted a series of growths at T_{sub} = 873 K, $pO_3 = 1.33 \times 10^{-4}$ Pa, varying only the overall growth time. Growth was interrupted at different stages to perform X-ray scattering and spectroscopy and study the evolution of the film as a function of film thickness. One film was grown without interruption (having the fastest effective deposition rate of 0.003 Å/s), a second was interrupted for measurement after deposition of every four bilayers (BLs) (with an intermediate deposition rate of 0.002 Å/s), while a third film was interrupted after deposition of every BL (with the slowest deposition rate of 0.001 Å/s). The scattered intensities at 0 0 1/2 rlu and growth/interruption schemes for these films are shown in Figure 5a, c, and e, where the observed oscillations correspond to the growth of each individual SrO-CoO_x bilayer. Since $SrCoO_{2.5}$ exhibits a distinct Bragg reflection at 001/2 rlu, (the (002) peak of $SrCoO_{2.5}$) as shown in Figure 1e, the appearance of the brownmillerite phase here should result in a gradual increase of intensity with deposition time; this behavior is observed unambiguously for growth of the two films with the faster overall deposition rates in Figure 5a and c. For both films, the brownmillerite phase does not appear until after the deposition of eight BLs. The brownmillerite crystal structure requires a minimum of four BLs for a unit cell (which should result in a weak but discernible Bragg peak at (001/2) rlu, as shown in Figure 1a), indicating that there is a two-unit-cell critical thickness for brownmillerite phase formation. As will be discussed below, cobalt is already in the 3+ oxidation state at four BLs; thus, the film indeed has composition $SrCoO_{2.5}$ at this thickness but with a disordered vacancy arrangement on the oxygen sublattice. The intensity at the 0 0 1/2 rlu for the film that was interrupted the most frequently is weaker and its behavior is less predictable than the others, as shown in Figure 5e. The intensity also increases after the deposition of eight BLs but then reaches a plateau for the final four BLs of growth.

The final (00L) scans for these films are shown in Figure 5b, d, and f, which indicate that the films grown at faster deposition rates consist primarily of BM-SCO while the more slowly grown film is composed of both $SrCoO_{2.5}$ and $Sr_3Co_2O_{6\pm\delta}$. We therefore conclude that decomposition of the $SrCoO_{2.5}$ phase into $Sr_3Co_2O_{6\pm\delta}$ and CoO can be avoided by increasing the deposition rate, which is in good agreement with the results for PLD-grown films.[3,10] The consequences of these results in terms of thermodynamic theory predictions and kinetic models will be discussed further in later sections.

DOI: 10.1021/acsami.7b16970
ACS Appl. Mater. Interfaces 2018, 10, 5949–5958

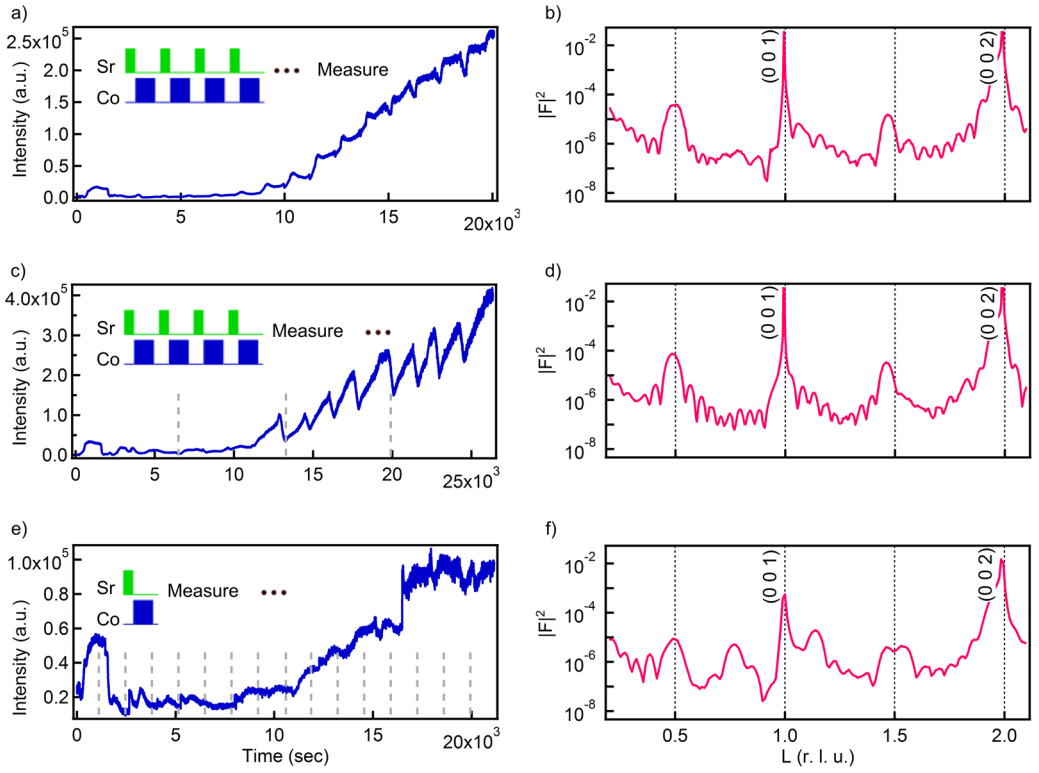

Figure 5. Scattered X-ray intensity at the (001/2) position during growth (left) of three different Sr−Co−O films (a, c, e) on $SrTiO_3$ (001) and their corresponding (00*L*) scans of the films (right) after growth (b, d, f). Films were interrupted (marked as "Measure") during growth as depicted in the inset shutter schematics of panels a, c, and e. All growths shown were conducted at T_{sub} = 873 K, pO_3 = 1.33 × 10^{-4} Pa.

Figure 6 shows the evolution in the (00*L*) scans as a function of film thickness for the BM-SCO film that was interrupted every four BL (Figure 6a, c) and the BM-SCO + 326-SCO film interrupted after every BL (Figure 6b, d); the tick marks on the right sides of Figure 6c and d indicate times at which a bilayer is deposited. It is clearly seen in Figure 6c that the half-order reflections at 001/2 and 003/2 rlu (indicated by the pink arrows) gain intensity after the deposition of eight BL. These peaks persist and become sharper as the film grows, as expected for an epitaxial film. For the two-phase film, shown in Figure 6d, reflections from the Ruddlesden−Popper phase near L = 0.77 and L = 1.14 (indicated by the blue arrows) become distinct from the thickness fringes after deposition of ∼5 BLs, in agreement with the $Sr_3Co_2O_{6\pm\delta}$ unit cell lattice constant of ∼2 nm. As with Figure 6c, intensity at the 001/2 r.l.u. of $SrCoO_{2.5}$ appears only after deposition of eight BLs. The Bragg peaks from both phases persist throughout growth and sharpen with increasing film thickness, indicating that the two phases' presence is set soon after the nucleation stage.

We fit the distinct $SrCoO_{2.5}$ and $Sr_3Co_2O_{6\pm\delta}$ Bragg peaks with Gaussian functions to find the full-width half maxima and determine the average thicknesses of each phase within the growing films (0.3905 nm/fwhm); instrumental broadening is considered insignificant based on the narrowness of the $SrTiO_3$ Bragg peaks. The total film thickness was determined from the spacing of the thickness fringes (0.3905 nm/Δ*L*). The results of this analysis are summarized in Figure 7a for the BM-SCO phase and Figure 7b for the two-phase film. The close match between the two curves in Figure 7a indicates that the out-of-plane correlation length of the $SrCoO_{2.5}$ spans the film thickness, as expected for a coherently strained film. The data in Figure 7b show that the BM-SCO and 326-SCO phases grew at similar rates, with final phase thicknesses equal to that of the total film thickness. This indicates that a simple domain structure for this film is represented by a self-assembled vertically aligned *nanocomposite* comprising the $Sr_3Co_2O_{6\pm\delta}$ and $SrCoO_{2.5}$ phases.[54]

Results of the in situ XANES measurements for the single-phase BM-SCO and two-phase BM-SCO + 326-SCO films are shown in Figure 8a and b, respectively. After the growth of 16 BLs for each of the films, cobalt exhibited the 3+ oxidation state. Interestingly, for the BM-SCO film in Figure 8a, the 3+ oxidation state is present from the start, even after the growth of only four BL. Since the brownmillerite structure does not form until after the deposition of eight BL (as discussed above), this indicates that the oxygen vacancy concentration is already set at four BL. There is negligible change in the shape of the XANES profile as the $SrCoO_{2.5}$ continues to grow.

As for the composite film shown in Figure 8b, the first grown layer of cobalt oxide appears to be CoO, possibly from a tetrahedrally coordinated layer, as discussed by Meyer et al.[55] According to the brownmillerite structure shown in Figure 1a, the subsequent cobalt oxide layer is CoO_2, such that the average Co oxidation state should be 3+ after two BLs. Similarly, from the $Sr_3Co_2O_{6\pm\delta}$ structure shown in Figure 4b, each cobalt oxide plane consists of Co_3O_5, such that the Co should be 3+ or higher, from the start of deposition. Here, however, every subsequent CoO_x layer appears to increase its average oxygen coordination until cobalt reaches Co^{3+} at ∼14 BLs. The reason for composite formation may be related to the redistribution of oxygen vacancies. As the brownmillerite phase exhibits long-range vacancy ordering, the deviation of oxygen stoichiometry from 2.5 cannot be too large (as demonstrated in Figure 8a). Therefore, excess oxygen vacancies in the initial

DOI: 10.1021/acsami.7b16970
ACS Appl. Mater. Interfaces 2018, 10, 5949−5958

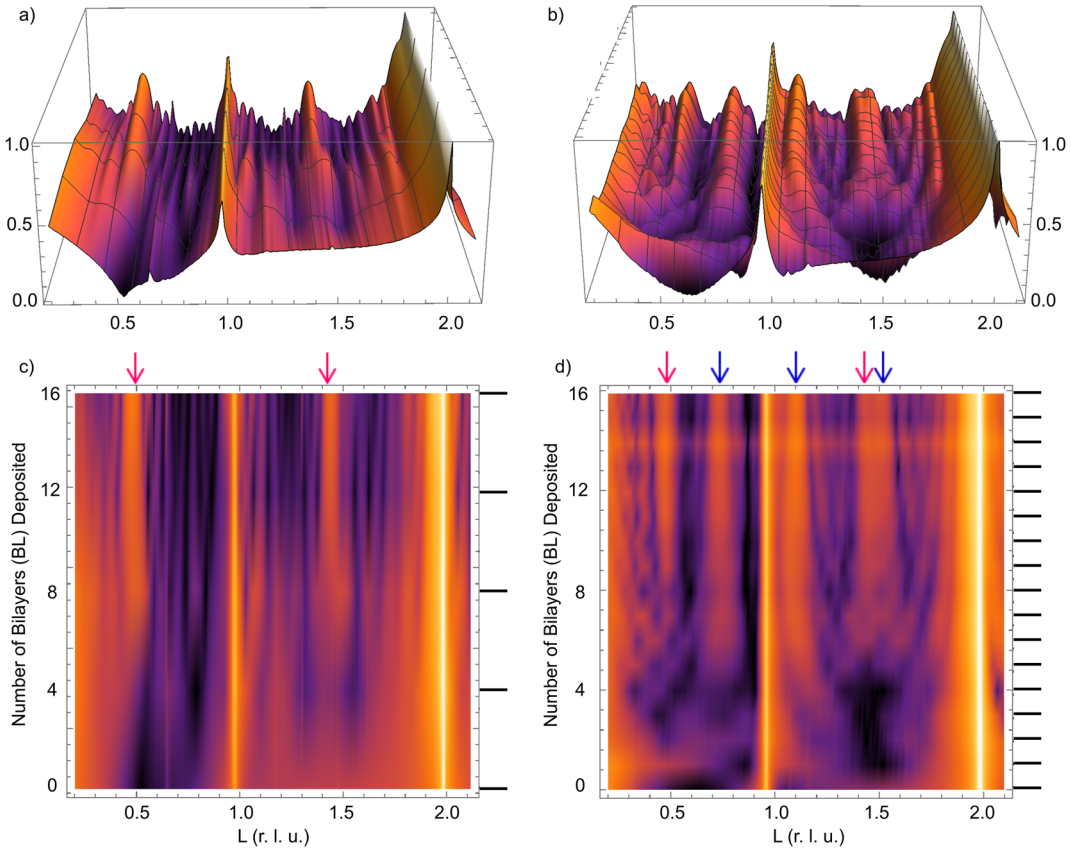

Figure 6. Scattering X-ray intensity along the (00*L*) specular rod showing evolution of the film structure for films interrupted after deposition of each four BLs (a, c) or interrupted every BL (b, d). All intensities (*z*-axis and color map lightness) are plotted on a normalized $\log_{10}$ scale. Arrows in panels c and d indicate peak positions characteristic to the BM-SCO (pink) and 326-SCO (blue) phases while tick marks on the right axis indicate when measurements were taken.

nuclei of $SrCoO_{2.5}$ may be redistributed laterally to structures that can tolerate a greater concentration of oxygen vacancies, such as $Sr_3Co_2O_{6-\delta}$.[50] This would lead to the formation of a nanocomposite where the phase fraction of $Sr_3Co_2O_{6-\delta}$ increases in more reducing growth conditions.

Thermodynamics of Sr−Co−O Film Growth. The microstructure of the strontium cobaltite films grown by MBE appears to depend strongly on the growth rate. For the series of growths discussed, fast growth (relative to atomic diffusion) results in stabilization of the $SrCoO_{2.5}$ phase, while slow growth leads to a mixture of $SrCoO_{2.5}$ and $Sr_3Co_2O_{6\pm\delta}$. This indicates that altering the effective deposition rate of films via MBE allows selection of the phase fraction with regions dominated by either kinetics or thermodynamics.

To probe the underlying mechanisms governing the formation of the observed phases, available thermodynamic data for the Sr−Co−O system were compared to the results of a series of growth experiments in different conditions with an identical A:B ratio and shutter sequence as described in the experimental section.

The SCO films grown using O_2 and O_3 can be directly compared as outlined by Suzuki et al.,[56] using the thermodynamic quantity of oxygen activity in ozone, a_{O_2}. Chemical equilibrium between ozone and oxygen gas is given by $O_3(g) \leftrightarrow 3/2O_2(g)$, so the standard Gibbs free energy change for ozone decomposition is

$$\Delta G^\circ = -RT\ln\frac{(p_{O_2}^{eq})^{3/2}}{p_{O_3}^{eq}}$$

where R is the gas constant, T is the temperature, and p_{O_2} and p_{O_3} are the equilibrium partial pressures of oxygen and ozone. This can be rewritten in terms of the thermochemical activity of oxygen in ozone (a_{O_2}) as

$$\Delta G^\circ = -RT\ \ln\frac{(a_{O_2}P^\circ)^{3/2}}{p_{O_3}}$$

where P° is the total gas pressure of the system. Since Sr/Co = 1, the oxygen partial pressure for 326-SCO ($Sr_3Co_2O_6$, taken as $Sr_9Co_6O_{18}$ in thermodynamic equations) and brownmillerite (BM-SCO, $SrCoO_{2.5}$, taken as $Sr_2Co_2O_5$ in thermodynamic equations) phase coexistence, $p_{O_2}^{eq}$(326-SCO ↔ BM-SCO), can be determined from the reaction $4Sr_9Co_6O_{18}$(326-SCO) + 12CoO + $3O_2$(g) ↔ $18Sr_2Co_2O_5$(BM-SCO). The free energy of $Sr_2Co_2O_5$ (BM) formation is then given by

$$G_f^\circ = -RT\ \ln\frac{a_{BM\text{-}SCO}^{18}}{a_{326\text{-}SCO}^{4}a_{CoO}^{12}(p_{O_2}^{eq}(326\text{-}SCO \leftrightarrow BM\text{-}SCO))^3}$$

where $a_{BM\text{-}SCO}$, $a_{326\text{-}SCO}$, and a_{CoO} are the activities of these materials relative to the pure substances. Assuming these activities to be unity, p_{O_2}(326-SCO ↔ BM-SCO) can be calculated for this reaction in the experimental temperature

DOI: 10.1021/acsami.7b16970
ACS Appl. Mater. Interfaces 2018, 10, 5949−5958

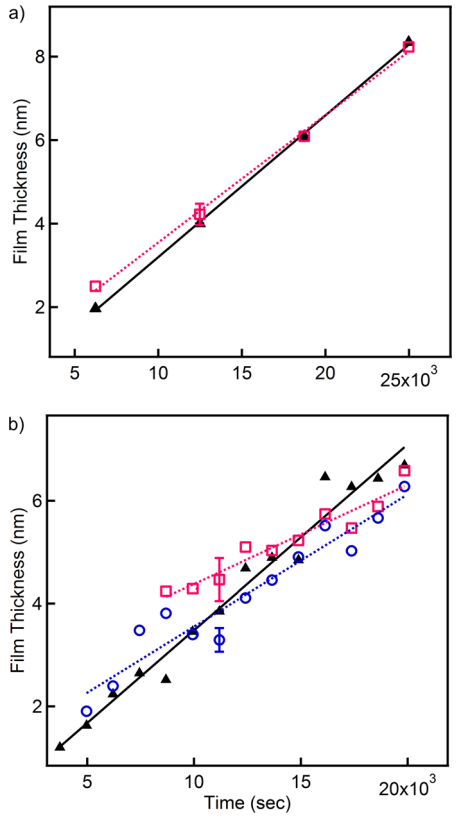

Figure 7. Thickness of different phases during growth in a pure BM-SCO film (a) and the BM-SCO + 326-SCO film (b). The BM-SCO phase is indicated by the pink traces, and the 326-SCO phase is indicated by the blue traces, while the overall film thickness based on CTR thickness fringes is indicated in black. Linear fits are drawn as a guide for the eye.

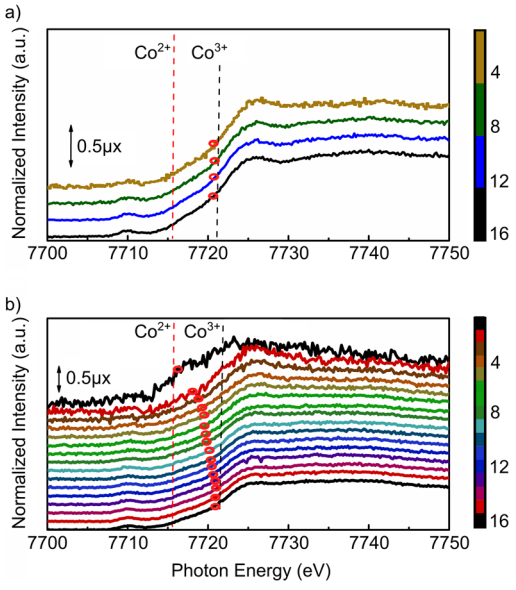

Figure 8. In situ XANES measured at the Co K-edge during growth of two films interrupted at different points throughout growth, showing a phase-pure BM-SCO film (a) interrupted after deposition of each four BL and a two-phase BM-SCO and 326-SCO film (b) interrupted after deposition of each BL.

range using thermodynamic constants found in recent literature.[45,53,57] We present calculations for p_{O_2}(326-SCO ↔ BM-SCO) and a_{O_2}(326-SCO ↔ BM-SCO) in Figure 9a. Here, the temperature dependent activities of 100% O_3 and 100% O_2 at 1.33×10^{-4} Pa, that is, the most oxidizing and most reducing conditions used in these experiments, are shown as short and long dashed lines, respectively. As depicted, growth in an atmosphere of 100% O_2 gas ($a_{O_2} = 1.3 \times 10^{-9}$ compared to a_{O_2} at 101,325 Pa) should yield the brownmillerite phase for T_{sub} < 345 K, a temperature too low to achieve good crystal quality. Above this temperature, 326-SCO and CoO are thermodynamically favored. However, if 100% O_3 gas is used, the BM-SCO is favored up to a growth temperature of 835 K.

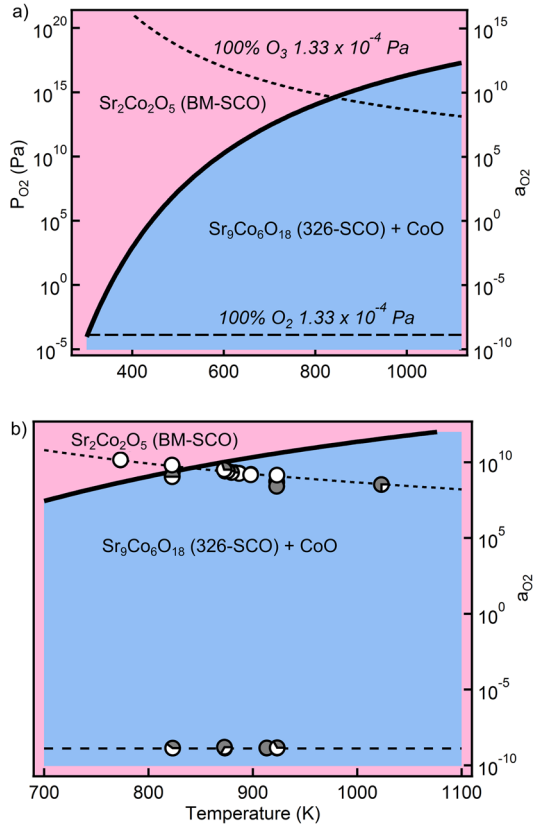

Figure 9. Thermodynamic phase diagram (a) showing p_{O_2}/a_{O_2} (left/right axis) for the 326-SCO ↔ BM-SCO reaction (bold line). The a_{O_2} of 100% O_3 at 1.33×10^{-4} Pa is indicated as a short, dashed line, while 100% O_2 at 1.33×10^{-4} Pa is indicated by the long, dashed line. In panel b, containing an enlarged view of panel a, we overlay the results for films of Sr−Co−O grown at varying T_{sub} and a_{O_2}. Open and dark circles indicate brownmillerite and 326-SCO films, respectively, with mixtures of the two indicated by partially shaded circles.

The data from growth experiments are overlaid on this plot in Figure 9b. To the left and above the solid a_{O_2}(326-SCO ↔ BM-SCO) boundary, only the brownmillerite phase is present (indicated by the open circles), as predicted by thermodynamics. However, to the right and below this line, the phase behavior of the Sr−Co−O system becomes more complex as shown by partially shaded circles; here, more shading corresponds to a greater $Sr_3Co_2O_{6\pm\delta}$ phase fraction. Contrary to the thermodynamics, films of pure BM-SCO, pure 326-SCO, or a mixture of the two can be grown in this region. From the

DOI: 10.1021/acsami.7b16970
ACS Appl. Mater. Interfaces 2018, 10, 5949−5958

experiments summarized in Figure 9b, stabilizing the $SrCoO_{2.5}$ phase outside of its thermodynamically stable phase region was challenging despite controlling the Sr:Co ratio and shuttering scheme. This chemical analysis considers only thermodynamics while ignoring interface energies, epitaxial strain, and kinetic effects, which can be critical to thin film phase stability. For example, higher quality epitaxial films of $SrCoO_{2.5}$ have been grown on LSAT, lanthanum aluminate−strontium aluminum tantalite, than on $SrTiO_3$, due to the better lattice mismatch with $SrCoO_{2.5}$.[3] These calculations nevertheless provide insight into the energetics of film growth, which is apparent from the relative agreement seen in Figure 9b. The three open circles just inside the 326-SCO region refer to films grown at effectively faster rates, displaying the kinetically stabilized Brownmillerite structure. The agreement is more evident if growth is performed in a region far from the BM-SCO ↔ 326-SCO phase boundary, where the thermodynamically stable phase is favored, for example when 100% O_2 is used rather than O_3 during synthesis (bottom of Figure 9b). This is illustrated by the series of films interrupted during growth to produce different effective growth rates, V_E. These three growths were conducted just inside the 326-SCO phase region. The growth of the mixed-phase films indicates that above some critical growth velocity, V_c, metal atoms deposited do not experience sufficient surface diffusion, D_s, to nucleate the thermodynamically stable phase.

Kinetics of Sr−Co−O Film Growth. Slower growth of films led to increased observation of the expected thermodynamic phase, while faster growth stabilized the brownmillerite phase- implying kinetic control. This agrees qualitatively with two models proposed in the literature for MBE growth. The first model, based on alloy decomposition,[58−60] states that growth temperature, rate, epitaxial strain, and thermal expansion coefficients of the phases determine the stable phases and morphology of films. The effects of temperature and growth velocity, as well as the vertical domain structure are consistent with our experimental observations. Epitaxial strain is likely to be very important in the energetics of the Sr−Co−O system, as films grown on LSAT (001)-oriented substrates under similar conditions displayed stability of the BM-SCO phase well into the unstable thermodynamic region. This is most likely due to differences in the degree of lattice mismatch.

A more quantitative second model consistent with our observations is solute trapping. This model is valid when the brownmillerite growth rate prevents atoms from migrating to their thermodynamically favored positions.[30−33] Solute trapping thus occurs under the condition

$$\frac{Va}{D} > 1$$

where V = growth velocity, a = hopping distance, and D = interface diffusion coefficient. Here, a high film growth rate implies that the resulting phase depends on the metal source shutter sequence and timing, leading to A−B cation substitution as atoms are quickly "frozen" in place by the advancing growth front. For the series of films grown with different V_E, the ratio $(V\,a)/D$ can be underestimated using the self-diffusion coefficient of cobalt in cobalt $D_{Coself} = 3.03 \times 10^{-18}$ cm^2/s (ref 61) and $a_{Co-Co} \cong 3$ Å. The growth velocity for these films ranged from 0.001−0.003 Å/s, resulting in $(V\,a)/D \cong 0.1-0.3$. This is an underestimate, as the self-diffusion coefficient in the oxide is certainly smaller than that of the metal, and a value of 3 Å for the hopping distance is likely too small. At these ratios, particularly those closer to one, it is likely that the process of solute trapping occurs, thereby allowing films to retain the BM-SCO structure.

CONCLUSIONS

Our results on the layer-by-layer growth by oxide MBE of the Sr−Co−O oxide system provide insight into the different roles of thermodynamics and kinetics on complex oxide phase stability. It was observed that while $SrCoO_{2.5}$ can be stabilized by both epitaxial strain and faster growth rates, longer exposures to high temperature/low oxygen activity environments help to stabilize the $Sr_3Co_2O_{6\pm\delta}$ phase, and moderate growth rates in these conditions can lead to the self-assembly of an epitaxial nanocomposite. The phase formation is in semiquantitative agreement with the established theory of solute trapping. Combining thermodynamic phase diagram calculations, where data on the relevant phases is available, with experimental investigation of a wide range of growth conditions is an approach that should be applied to other complex oxide systems. Insight from this approach leads to effective strategies for targeting the formation of other desirable oxide phases or phase mixtures similar to those observed in the Sr−Co−O system.

The brownmillerite phase of $SrCoO_{2.5}$ was observed to require a minimum thickness of two unit cells; the oxygen vacancies remained disordered below this thickness. The in situ XANES data showed that Co reaches the 3+ oxidation state for a single unit cell and remains fixed for the remainder of deposition. In contrast, $Sr_3Co_2O_{6-\delta}$ nucleates with some oxygen deficiency, δ, gradually incorporating more oxygen from the environment during growth.

As demonstrated, investigating the effects of deposition rate on phase behavior in the MBE environment necessitates the use of in situ probes, particularly when dealing with oxygen-deficient materials and attempting to understand the thermodynamic and kinetic contributors to growth behavior. This investigation into the Sr−Co−O system, with its highly flexible oxidation state and rich phase diagram, provides a prototypical example for understanding the synthesis of other multivalent transition metal oxides. We show that both X-ray scattering and spectroscopy are key to revealing the physical and chemical processes taking place during deposition and that such in situ techniques are essential for optimizing the defect-engineered properties of cobaltite heterostructures.

AUTHOR INFORMATION

Corresponding Author

*E-mail: TassieAndersen2013@u.northwestern.edu.

ORCID

Tassie K. Andersen: 0000-0002-9544-4995

Author Contributions

The manuscript was written through contributions of all authors. All authors have given approval to the final version of the manuscript.

Notes

The authors declare no competing financial interest.

ACKNOWLEDGMENTS

Work performed at Argonne National Laboratory, including the Advanced Photon Source, was supported by the U.S. Department of Energy (DOE), Basic Energy Sciences, under Contract No. DE-AC02-06CH11357.

DOI: 10.1021/acsami.7b16970
ACS Appl. Mater. Interfaces 2018, 10, 5949−5958

REFERENCES

(1) Wachsman, E.; Lee, K. Lowering the Temperature of Solid Oxide Fuel Cells. *Science* **2011**, *334*, 935−939.

(2) Feng, Z.; Hong, W.; Fong, D. D.; Lee, Y.; Yacoby, Y.; Morgan, D.; Shao-Horn, Y. Catalytic Activity and Stability of Oxides: The Role of Near-Surface Atomic Structures and Compositions. *Acc. Chem. Res.* **2016**, *49*, 966−973.

(3) Jeen, H. J.; Choi, W. S.; Biegalski, M. D.; Tung, I. C.; Shin, D.; Ohta, H.; Chisholm, M. F.; Lee, H. N.; et al. Reversible Redox Reactions in an Epitaxially Stabilized $SrCoO_x$ Oxygen Sponge. *Nat. Mater.* **2013**, *12*, 1057−1063.

(4) Mefford, J. T.; et al. Water Electrolysis on $La_{1-x}Sr_xCoO_{3-\delta}$ Perovskite Electrocatalysts. *Nat. Commun.* **2016**, *7*, 11053.

(5) Cavin, R. K.; Lugli, P.; Zhirnov, V. V. Science and Engineering Beyond Moore's Law. *Proc. IEEE* **2012**, *100*, 1720−1749.

(6) Zhou, Y.; Ramanathan, S. Mott Memory and Neuromorphic Devices. *Proc. IEEE* **2015**, *103* (8), 1289−1310.

(7) Zubko, P.; Gariglio, S.; Gabay, M.; Ghosez, P.; Triscone, J.-M. Interface Physics in Complex Oxide Heterostructures. *Annu. Rev. Condens. Matter Phys.* **2011**, *2* (1), 141−165.

(8) Spaldin, N. A.; Fiebig, M. The Renaissance of Magnetoelectric Multiferroics. *Science* **2005**, *309* (5733), 391−392.

(9) Kalinin, S. V.; Borisevich, A.; Fong, D. Beyond Condensed Matter Physics on the Nanoscale: The Role of Ionic and Electrochemical Phenomena in the Physical Functionalities of Oxide Materials. *ACS Nano* **2012**, *6* (12), 10423−10437.

(10) Jeen, H.; Bi, Z.; Choi, W. S.; Chisholm, M. F.; Bridges, C. A.; Paranthaman, M. P.; Lee, H. N. Orienting Oxygen Vacancies for Fast Catalytic Reaction. *Adv. Mater. (Weinheim, Ger.)* **2013**, *25* (44), 6459−6463.

(11) Lee, Y.-l.; Kleis, J.; Rossmeisl, J.; Shao-horn, Y.; Morgan, D. Prediction of Solid Oxide Fuel Cell Cathode Activity with First-Principles Descriptors. *Energy Environ. Sci.* **2011**, *4* (10), 3966−3970.

(12) Lu, Q.; Yildiz, B. Voltage-Controlled Topotactic Phase Transition in Thin-Film $SrCoO_x$ Monitored by In-Situ X-ray Diffraction. *Nano Lett.* **2016**, *16* (2), 1186−1193.

(13) Ezbiri, M.; Allen, K. M.; Gàlvez, M. E.; Michalsky, R.; Steinfeld, A. Design Principles of Perovskites for Thermochemical Oxygen Separation. *ChemSusChem* **2015**, *8* (11), 1966−1971.

(14) Xie, C. K.; Nie, Y. F.; Wells, B. O.; Budnick, J. I.; Hines, W. A.; Dabrowski, B. Magnetic Phase Separation in $SrCoO_x$ ($2.5 \leq x \leq 3$). *Appl. Phys. Lett.* **2011**, *99* (5), 052503.

(15) Lee, Y.-L.; Lee, D.; Wang, X. R.; Lee, H. N.; Morgan, D.; Shao-Horn, Y. Kinetics of Oxygen Surface Exchange on Epitaxial Ruddlesden−Popper Phases and Correlations to First-Principles Descriptors. *J. Phys. Chem. Lett.* **2016**, *7* (2), 244−249.

(16) Sun, C.; Hui, R.; Roller, J. Cathode Materials for Solid Oxide Fuel Cells: A Review. *J. Solid State Electrochem.* **2010**, *14* (7), 1125−1144.

(17) Tarancón, A.; Burriel, M.; Santiso, J.; Skinner, S. J.; Kilner, J. A. Advances in Layered Oxide Cathodes for Intermediate Temperature Solid Oxide Fuel Cells. *J. Mater. Chem.* **2010**, *20* (19), 3799−3813.

(18) Long, Y.; Kaneko, Y.; Ishiwata, S.; Taguchi, Y.; Tokura, Y. Synthesis of Cubic $SrCoO_3$ Single Crystal and its Anisotropic Magnetic and Transport Properties. *J. Phys.: Condens. Matter* **2011**, *23* (24), 245601.

(19) Ichikawa, N.; Iwanowska, M.; Kawai, M.; Calers, C.; Paulus, W.; Shimakawa, Y. Reduction and Oxidation of $SrCoO_{2.5}$ Thin Films at Low Temperatures. *Dalton Trans.* **2012**, *41* (35), 10507−10510.

(20) Le Toquin, R.; Paulus, W.; Cousson, A.; Prestipino, C.; Lamberti, C. Time-Resolved In-Situ Studies of Oxygen Intercalation into $SrCoO_{2.5}$, Performed by Neutron Diffraction and X-ray Absorption Spectroscopy. *J. Am. Chem. Soc.* **2006**, *128* (40), 13161−13174.

(21) Lu, N.; et al. Electric-Field Control of Tri-State Phase Transformation with a Selective Dual-Ion Switch. *Nature* **2017**, *546* (7656), 124−128.

(22) Tambunan, O. T.; Parwanta, K. J.; Acharya, S. K.; Lee, B. W.; Jung, C. U.; Kim, Y. S.; Park, B. H.; Jeong, H.; Park, J.-Y.; Cho, M. R.; Park, Y. D.; Choi, W. S.; Kim, D.-W.; Jin, H.; Lee, S.; Song, S. J.; Kang, S.-J.; Kim, M.; Hwang, C. S. Resistance Switching in Epitaxial $SrCoO_x$ Thin Films. *Appl. Phys. Lett.* **2014**, *105* (6), 063507.

(23) Karvonen, L.; Yamauchi, H.; Karppinen, M. Homologous Series of $SrCoO_{(3n-1)/n}$ Perovskites Obtained Through Br_2 Oxygenation of $SrCoO_{2.5}$. *Chem. Mater.* **2008**, *20* (22), 7143−7147.

(24) Hodges, J. P.; Short, S.; Jorgensen, J. D.; Xiong, X.; Dabrowski, B.; Mini, S. M.; Kimball, C. W. Evolution of Oxygen-Vacancy Ordered Crystal Structures in the Perovskite Series $Sr_nFe_nO_{3n-1}$ (n= 2, 4, 8, and ∞), and the Relationship to Electronic and Magnetic Properties. *J. Solid State Chem.* **2000**, *151* (2), 190−209.

(25) Christen, H. M.; Eres, G. Recent Advances in Pulsed-Laser Deposition of Complex Oxides. *J. Phys.: Condens. Matter* **2008**, *20* (26), 264005.

(26) Willmott, P. R.; Huber, J. R. Pulsed Laser Vaporization and Deposition. *Rev. Mod. Phys.* **2000**, *72* (1), 315−328.

(27) Baiutti, F.; Gregori, G.; Wang, Y.; Suyolcu, Y. E.; Cristiani, G.; Van Aken, P. A.; Maier, J.; Logvenov, G. Cationic Redistribution at Epitaxial Interfaces in Superconducting Two-Dimensionally Doped Lanthanum Cuprate Films. *ACS Appl. Mater. Interfaces* **2016**, *8* (40), 27368−27375.

(28) Schlom, D. G. Perspective: Oxide Molecular-Beam Epitaxy Rocks! *APL Mater.* **2015**, *3* (6), 062403.

(29) Lee, J. H.; Luo, G.; Tung, I. C.; Chang, S. H.; Luo, Z.; Malshe, M.; Gadre, M.; Bhattacharya, A.; Nakhmanson, S. M.; Eastman, J. A.; Hong, H.; Jellinek, J.; Morgan, D.; Fong, D. D.; Freeland, J. W. Dynamic Layer Rearrangement During Growth of Layered Oxide Films by Molecular Beam Epitaxy. *Nat. Mater.* **2014**, *13* (9), 879−883.

(30) Aziz, M. Interface Attachment Kinetics in Alloy Solidification. *Metall. Mater. Trans. A* **1996**, *27* (3), 671−686.

(31) Baker, J.; Gahn, J. Solute trapping by rapid solidification. *Acta Metall.* **1969**, *17* (5), 575−578.

(32) Boettinger, W. J.; Perepezko, J. H. *Fundamentals of Rapid Solidification*; 1985.

(33) Han, X.; Spencer, B. J. A Nonlinear Model for Surface Segregation and Solute Trapping During Planar Film Growth. *J. Appl. Phys. (Melville, NY, U. S.)* **2007**, *101* (8), 084302.

(34) Koster, G.; Kropman, B. L.; Rijnders, G. J. H. M.; Blank, D. H. A.; Rogalla, H. Quasi-ideal Strontium Titanate Crystal Surfaces Through Formation of Strontium Hydroxide. *Appl. Phys. Lett.* **1998**, *73* (20), 2920−2922.

(35) Eckstein, J. N.; Bozovic, I.; Von Dessonneck, K. E.; Schlom, D. G.; Harris, J. S., Jr; Baumann, S. M. Atomically Layered Heteroepitaxial Growth of Single-Crystal Films of Superconducting $Bi_2Sr_2Ca_2Cu_3O_x$. *Appl. Phys. Lett.* **1990**, *57* (9), 931−933.

(36) Eckstein, J. N.; Schlom, D. G.; Hellman, E. S.; Von Dessonneck, K. E.; Chen, Z. J.; Webb, C.; Turner, F.; Harris, J. S., Jr; Beasley, M. R.; Geballe, T. H. Epitaxial Growth of High-Temperature Superconducting Thin Films. *J. Vac. Sci. Technol., B: Microelectron. Process. Phenom.* **1989**, *7* (2), 319−323.

(37) Schlom, D. G.; Marshall, A. F.; Sizemore, J. T.; Chen, Z. J.; Eckstein, J. N.; Bozovic, I.; Von Dessonneck, K. E.; Harris, J. S.; Bravman, J. C. Molecular Beam Epitaxial Growth of Layered Bi-Sr-Ca-Cu-O Compounds. *J. Cryst. Growth* **1990**, *102* (3), 361−375.

(38) Lee, J. H.; Tung, I. C.; Chang, S. H.; Bhattacharya, A.; Fong, D. D.; Freeland, J. W.; Hong, H. In-Situ Surface/Interface X-ray Diffractometer for Oxide Molecular Beam Epitaxy. *Rev. Sci. Instrum.* **2016**, *87* (1), 013901.

(39) Stephenson, G. B.; Eastman, J. A.; Auciello, O.; Munkholm, A.; Thompson, C.; Fuoss, P. H.; Fini, P.; DenBaars, S. P.; Speck, J. S. Real-Time X-ray Scattering Studies of Surface Structure During Metal-organic Chemical Vapor Deposition of GaN. *MRS Bull.* **1999**, *24* (1), 21−25.

(40) Schlepütz, C. M.; Herger, R.; Willmott, P. R.; Patterson, B. D.; Bunk, O.; Brönnimann, C.; Henrich, B.; Hülsen, G.; Eikenberry, E. F. Improved Data Acquisition in Grazing-Incidence X-ray Scattering Experiments Using a Pixel Detector. *Acta Crystallogr., Sect. A: Found. Crystallogr.* **2005**, *61* (4), 418−425.

DOI: 10.1021/acsami.7b16970
ACS Appl. Mater. Interfaces 2018, 10, 5949−5958

(41) de La Calle, C.; Aguadero, A.; Alonso, J. A.; Fernández-Díaz, M. T. Correlation Between Reconstructive Phase Transitions and Transport Properties from $SrCoO_{2.5}$ Brownmillerite: A Neutron Diffraction Study. *Solid State Sci.* **2008**, *10* (12), 1924−1935.
(42) Muñoz, A.; de La Calle, C.; Alonso, J.; Botta, P.; Pardo, V.; Baldomir, D.; Rivas, J. Crystallographic and Magnetic Structure of $SrCoO_{2.5}$ Brownmillerite: Neutron Study Coupled with Band-Structure Calculations. *Phys. Rev. B: Condens. Matter Mater. Phys.* **2008**, *78* (5), 054404.
(43) Piovano, A.; Agostini, G.; Frenkel, A. I.; Bertier, T.; Prestipino, C.; Ceretti, M.; Paulus, W.; Lamberti, C. Time Resolved In-Situ XAFS Study of the Electrochemical Oxygen Intercalation in $SrFeO_{2.5}$ Brownmillerite Structure: Comparison with the Homologous $SrCoO_{2.5}$ System. *J. Phys. Chem. C* **2011**, *115* (4), 1311−1322.
(44) Sterbinsky, G. E.; Ryan, P. J.; Kim, J. W.; Karapetrova, E.; Ma, J. X.; Shi, J.; Woicik, J. C. Local Atomic and Electronic Structures of Epitaxial Strained $LaCoO_3$ Thin Films. *Phys. Rev. B: Condens. Matter Mater. Phys.* **2012**, *85* (2), 020403.
(45) Jankovský, O.; Sedmidubský, D.; Vítek, J.; Šimek, P.; Sofer, Z. Phase Diagram of the Sr−Co−O System. *J. Eur. Ceram. Soc.* **2015**, *35* (3), 935−940.
(46) Wang, X. L.; Sakurai, H.; Takayama-Muromachi, E. Synthesis, Structures, and Magnetic Properties of Novel Roddlesden-Popper Homologous Series $Sr_{n+1}Co_nO_{3n+1}$ (n = 1,2,3,4, and ∞). *J. Appl. Phys. (Melville, NY, U. S.)* **2005**, *97* (10), 10M519.
(47) Haeni, J. H.; Theis, C. D.; Schlom, D. G.; Tian, W.; Pan, X. Q.; Chang, H.; Takeuchi, I.; Xiang, X.-D. Epitaxial Growth of the First Five Members of the $Sr_{n+1}Ti_nO_{3n+1}$ Ruddlesden−Popper Homologous Series. *Appl. Phys. Lett.* **2001**, *78* (21), 3292−3294.
(48) Tian, W.; Haeni, J. H.; Schlom, D. G.; Hutchinson, E.; Sheu, B. L.; Rosario, M. M.; Schiffer, P.; Liu, Y.; Zurbuchen, M. A.; Pan, X. Q. Epitaxial Growth and Magnetic Properties of the First Five Members of the Layered $Sr_{n+1}Ru_nO_{3n+1}$ Oxide Series. *Appl. Phys. Lett.* **2007**, *90* (2), 022507.
(49) Tian, W.; Pan, X. Q.; Haeni, J. H.; Schlom, D. G. Transmission Electron Microscopy Study of n = 1−5 $Sr_{n+1}Ti_nO_{3n+1}$ Epitaxial Thin Films. *J. Mater. Res.* **2001**, *16* (7), 2013−2026.
(50) Dann, S. E.; Weller, M. T. Structure and Oxygen Stoichiometry in $Sr_3Co_2O_{7-y}$ ($0.94 \leq y \leq 1.22$). *J. Solid State Chem.* **1995**, *115* (2), 499−507.
(51) Viciu, L.; Zandbergen, H. W.; Xu, Q.; Huang, Q.; Lee, M.; Cava, R. J. Structure and Magnetic Properties of the Orthorhombic n= 2 Ruddlesden−Popper Phases $Sr_3Co_2O_{5+\delta}$ (δ= 0.91, 0.64 and 0.38). *J. Solid State Chem.* **2006**, *179* (2), 500−511.
(52) Nishio, K.; et al. Thermodynamic Guiding Principles in Selective Synthesis of Strontium Iridate Ruddlesden-Popper Epitaxial Films. *APL Mater.* **2016**, *4* (3), 036102.
(53) Zhang, W.-W.; Chen, M.; Povoden-Karadeniz, E.; Hendriksen, P. V. Thermodynamic Modeling of the Sr−Co−Fe−O System. *Solid State Ionics* **2016**, *292*, 88−97.
(54) Macmanus-Driscoll, J. L. Self-Assembled Heteroepitaxial Oxide Nanocomposite Thin Film Structures: Designing Interface-Induced Functionality in Electronic Materials. *Adv. Funct. Mater.* **2010**, *20* (13), 2035−2045.
(55) Meyer, T. L.; Jeen, H.; Gao, X.; Petrie, J. R.; Chisholm, M. F.; Lee, H. N. Symmetry-Driven Atomic Rearrangement at a Brownmillerite-Perovskite Interface. *Adv. Electron. Mater.* **2016**, *2*, 1500201.
(56) Suzuki, R. O.; Ogawa, T.; Ono, K. Use of Ozone to Prepare Silver Oxides. *J. Am. Ceram. Soc.* **1999**, *82* (8), 2033−2038.
(57) Chase, M. W. *NIST-JANAF Thermochemical Tables*, 4th ed.; NIST, 1998; Vol. *9*.
(58) Léonard, F.; Desai, R. Alloy Decomposition and Surface Instabilities in Thin Films. *Phys. Rev. B: Condens. Matter Mater. Phys.* **1998**, *57*, 4805−4815.
(59) Léonard, F.; Desai, R. Spontaneous Decomposition and Ordering During Epitaxial Growth. *Thin Solid Films* **1999**, *357* (1), 46−52.
(60) McCoy, M. A.; Grimes, R. W.; Lee, W. E. Phase Stability and Interfacial Structures in the SrO−$SrTiO_3$ System. *Philos. Mag. A* **1997**, *75* (3), 833−846.
(61) Bussmann, W.; Herzig, C.; Rempp, W.; Maier, K.; Mehrer, H. Isotope Effect and Self-Diffusion in Face-Centred Cubic cobalt. *Phys. Status Solidi A* **1979**, *56* (1), 87−97.

DOI: 10.1021/acsami.7b16970
ACS Appl. Mater. Interfaces 2018, 10, 5949−5958